

# Bidirectional Neural Networks for Global Nucleon-Nucleus Optical Model Calculations

Jin Lei<sup>1,\*</sup>

<sup>1</sup>*School of Physics Science and Engineering, Tongji University, Shanghai 200092, China.*

(Dated: December 30, 2025)

Modern nuclear data evaluation increasingly requires not only accurate scattering calculations, but also efficient methods for uncertainty quantification and parameter optimization, tasks that benefit from differentiable solvers amenable to gradient-based algorithms. I present a neural network emulator based on Bidirectional Liquid Neural Networks (BiLNN) that provides a fully differentiable mapping from optical potential parameters to scattering wave functions. The key innovation enabling generalization across the parameter space is the use of phase-space coordinates  $\rho = kr$  that normalize the oscillation wavelength regardless of projectile energy, allowing a single network to span 1 to 200 MeV. Trained on Numerov solutions for twelve target nuclei ( $^{12}\text{C}$  to  $^{208}\text{Pb}$ ), both protons and neutrons, and partial waves up to  $l = 30$ , the network achieves an overall relative error of 1.2%. The predicted wave functions yield accurate  $S$ -matrix elements and elastic scattering cross sections, reproducing diffraction patterns spanning four orders of magnitude. Importantly, the model extrapolates successfully to nuclei not included in training ( $^{24}\text{Mg}$ ,  $^{63}\text{Cu}$ ,  $^{184}\text{W}$ ) with comparable accuracy, demonstrating that it has learned the physics of the optical model rather than memorizing specific targets. The differentiable nature of the trained model opens the door to gradient-based optimization of optical model parameters and efficient uncertainty quantification.

## I. INTRODUCTION

Nuclear reactions are central to many areas of physics, from understanding the synthesis of elements in stars to applications in nuclear energy and medicine. When a nucleon, a proton or neutron, collides with an atomic nucleus, a variety of processes can occur: the nucleon may scatter elastically, preserving the internal state of both projectile and target; it may excite the target nucleus to higher energy levels; or it may be absorbed, leading to compound nucleus formation or other non-elastic channels. The relative probabilities of these outcomes, encoded in scattering cross sections, depend sensitively on the interaction between the incident nucleon and the target nucleus. Accurate theoretical predictions of these cross sections require a reliable description of the nucleon-nucleus potential and efficient methods for solving the resulting quantum mechanical scattering problem.

The optical model provides the standard theoretical framework for nucleon-nucleus scattering [1, 2]. The complex many-body interaction is replaced by an effective one-body potential with real and imaginary parts: the real part describes elastic scattering, while the imaginary part accounts for absorption into non-elastic channels. The potential is typically parameterized using Woods-Saxon functions with 10–20 adjustable parameters. Among the most widely used parameterizations is the Koning-Delaroche (KD02) potential [3], which describes both proton and neutron scattering on nuclei from magnesium to bismuth at energies from 1 keV to 200 MeV.

Given the optical potential, the scattering observables are obtained by solving the radial Schrödinger equation for each partial wave. The radial wave function must vanish at the origin and match to the appropriate asymptotic form, either Coulomb wave functions for charged particles or spherical Bessel functions for neutrons, at large distances where the nuclear potential vanishes. From this asymptotic matching, the scattering matrix element is extracted, and the elastic scattering angular distribution and reaction cross section follow from standard partial-wave expressions [4].

The standard numerical approach for solving the radial Schrödinger equation is the Numerov algorithm, a fourth-order finite-difference method that is highly accurate and stable. However, the Numerov algorithm, like all traditional numerical integrators, is fundamentally a discrete, step-by-step procedure that cannot be naturally embedded into modern gradient-based optimization frameworks. This limitation becomes significant as nuclear physics increasingly adopts inverse problem methodologies, where one seeks to infer potential parameters from experimental observables.

The limitations of traditional numerical methods become acute in the context of modern nuclear physics research. Next-generation radioactive beam facilities such as FRIB and FAIR are producing data on nuclei far from stability, requiring optical model predictions for systems where experimental constraints are sparse [5, 6]. Nuclear astrophysics demands reaction rates for thousands of nuclei across wide energy ranges to model stellar nucleosynthesis [7]. Meanwhile, rigorous uncertainty quantification has become essential for nuclear data applications, requiring systematic exploration of high-dimensional parameter spaces through Bayesian inference [8, 9]. These developments call for solvers that are not merely fast, but *differentiable*, enabling gradients of observables with re-

---

\* jinl@tongji.edu.cn

spect to potential parameters to be computed efficiently through automatic differentiation.

Machine learning offers precisely this capability. A neural network that maps potential parameters to wave functions is inherently differentiable: gradients flow seamlessly from the output wave function back through the network to the input parameters via the chain rule. This enables end-to-end gradient-based optimization, where experimental cross sections can directly constrain optical model parameters without resorting to derivative-free methods such as Markov Chain Monte Carlo or simplex algorithms. The neural network thus serves not as a faster replacement for Numerov, but as a qualitatively different computational object, a *differentiable surrogate* that bridges the gap between forward modeling and inverse inference. Beyond differentiability, neural networks can discover and exploit regularities in the solution space. If the optical model captures genuine physical universality, as suggested by the success of global parameterizations, then a well-designed network should learn this universality and generalize to new nuclei not seen during training.

Neural networks have been applied successfully to various problems in nuclear physics, including predictions of nuclear masses [10] and level densities [11]. Physics-informed approaches have emerged as powerful tools for solving differential equations [12, 13], and specialized architectures have been developed for quantum mechanical problems [14, 15]. However, applying these methods to scattering wave functions presents unique challenges.

A significant challenge in applying neural networks to the scattering problem is the wide range of length scales involved. The de Broglie wavelength of the projectile varies from approximately 9 fm at 10 MeV to about 2 fm at 200 MeV, a factor of 4.5 variation across the energy range of interest. A network trained to predict wave functions as a function of the radial coordinate would need to learn oscillatory patterns with vastly different periods at different energies, a task that proves difficult in practice. Moreover, the wave function amplitude can vary over several orders of magnitude due to absorption effects from the imaginary potential, adding another layer of complexity.

In this work, I address these challenges by developing a neural network architecture specifically designed for the nucleon-nucleus scattering problem. Two key innovations enable generalization across the full parameter space of energies, partial waves, and target nuclei. First, I introduce *phase-space coordinates* that absorb the energy dependence of the wavelength: in this representation, the wave function oscillates with a universal period regardless of energy, dramatically simplifying the learning task. Second, I employ a *Bidirectional Liquid Neural Network* (BiLNN) based on Closed-form Continuous-time (CfC) layers [16], which process the radial coordinate sequence in both forward and backward directions. This bidirectional architecture naturally incorporates the two boundary conditions that define the scattering problem: the

wave function vanishing at the origin and the asymptotic Coulomb behavior at large distances.

The network is trained on wave functions computed using the Numerov method with the KD02 optical potential. The training set spans twelve target nuclei from  $^{12}\text{C}$  to  $^{208}\text{Pb}$ , both proton and neutron projectiles, energies uniformly sampled from 1 to 200 MeV, and partial waves from 0 to 30. This comprehensive coverage ensures that the trained network can interpolate reliably across the full parameter space relevant for practical applications. The network reproduces the Numerov wave functions with an average relative error of 1.2% across the training domain. The trained model provides a fast, differentiable surrogate suitable for applications in Bayesian inference and sensitivity analysis.

The paper is organized as follows. Section II presents the theoretical framework for nucleon-nucleus scattering, including the optical model potential and the Schrödinger equation. Section III describes the neural network architecture, the phase-space coordinate representation, and the training procedure. Results for wave function predictions and scattering observables are presented in Sec. IV. Finally, conclusions and an outlook for future developments are given in Sec. V.

## II. THEORETICAL FRAMEWORK

The scattering of a nucleon from a nucleus is described by the radial Schrödinger equation

$$\frac{d^2 u_l}{dr^2} + \left[ k^2 - U(r) - \frac{l(l+1)}{r^2} \right] u_l(r) = 0, \quad (1)$$

where  $u_l(r)$  is the radial wave function for partial wave  $l$ ,  $k = \sqrt{2\mu E}/\hbar$  is the asymptotic wave number with reduced mass  $\mu$  and center-of-mass energy  $E$ , and  $U(r) = 2\mu V(r)/\hbar^2$  is the reduced potential. The solution must satisfy the boundary conditions

$$u_l(r) \rightarrow 0 \quad \text{as } r \rightarrow 0, \quad (2)$$

$$u_l(r) \rightarrow H_l^{(-)}(\eta, kr) - S_l H_l^{(+)}(\eta, kr) \quad \text{as } r \rightarrow \infty, \quad (3)$$

where  $H_l^{(\pm)}$  are the Coulomb-Hankel functions with Sommerfeld parameter  $\eta = Z_1 Z_2 e^2 \mu / (\hbar^2 k)$ , and  $S_l$  is the scattering matrix element for partial wave  $l$ . For neutrons,  $\eta = 0$  and the Coulomb functions reduce to Riccati-Hankel functions.

The nucleon-nucleus optical model potential  $V(r)$  consists of real and imaginary parts describing elastic scattering and absorption, respectively. I employ the central terms of the global Koning-Delaroche (KD02) parameterization [3], which takes the form

$$V(r) = V_V(r) + V_S(r) + V_C(r), \quad (4)$$

where  $V_V$  is the volume term,  $V_S$  is the surface term, and  $V_C$  is the Coulomb potential for protons. Each term has

both real and imaginary components with Woods-Saxon or derivative Woods-Saxon radial forms. The spin-orbit term  $V_{SO}$  is not included in this work, as it would require treating spin-up and spin-down channels separately, significantly complicating the neural network architecture. For spin-zero targets and unpolarized beams, the spin-orbit contribution to the total cross section is small, making this a reasonable approximation for this initial study. The KD02 potential provides energy-dependent parameters fitted to extensive elastic scattering data for  $A = 24$ – $209$  nuclei at energies from 1 keV to 200 MeV. The potential depths and geometry parameters vary smoothly with energy and target mass, enabling interpolation to nuclei and energies not included in the original fit. In this work, I extend the KD02 parameterization to lighter nuclei such as  $^{12}\text{C}$  by extrapolating the smooth mass dependence, which allows training the network over a broader range of nuclear sizes.

I solve Eq. (1) numerically using the Numerov method with step size  $h = 0.05$  fm. The S-matrix is extracted by matching the numerical solution to Coulomb functions at  $r_{\text{match}} = 15$  fm.

### III. NEURAL NETWORK ARCHITECTURE

A neural network can be viewed as a highly flexible parameterization of a nonlinear function, conceptually similar to how a Fourier series or a set of basis functions represents a function, but with the basis functions themselves being learned from data. The basic operation is a linear transformation followed by a nonlinear function:

$$\mathbf{y} = \sigma(\mathbf{W}\mathbf{x} + \mathbf{b}), \quad (5)$$

where  $\mathbf{W}$  is a matrix of adjustable parameters (analogous to expansion coefficients),  $\mathbf{b}$  is a bias vector, and  $\sigma$  is a fixed nonlinear function. By composing many such transformations in sequence, forming a “deep” network, one can represent essentially any continuous mapping [17]. The key advantage over traditional basis expansions is that the network automatically discovers which features of the input are relevant for predicting the output.

The parameters  $\mathbf{W}$  and  $\mathbf{b}$  are determined by minimizing a cost function that measures the discrepancy between network predictions and known solutions. This optimization is performed using gradient descent, where the gradients are computed efficiently via the chain rule. Starting from random initial values, the parameters are iteratively updated until the cost function converges to a minimum.

For the scattering problem, the goal is to learn a mapping from the optical potential  $V(r)$  and physical parameters (energy  $E$ , partial wave  $l$ , target mass  $A$ ) to the radial wave function  $u_l(r)$ . In essence, the trained neural network serves as a surrogate Schrödinger equation solver: given the potential and boundary conditions as input, it directly outputs the wave function solution, bypassing the step-by-step numerical integration entirely.

This is analogous to having a lookup table that interpolates between pre-computed solutions, but with the interpolation scheme learned automatically from the structure of the problem. Crucially, this approach learns the scattering *wave function*  $u_l(r)$  rather than directly predicting observables such as cross sections or S-matrix elements. This distinction is significant: the wave function is the fundamental quantum mechanical object from which all observables can be derived, and it encodes richer physical information than any single observable. Learning the wave function means the network serves as a surrogate Schrödinger equation solver, capturing the full quantum mechanical structure of the scattering process. Observable quantities like cross sections, phase shifts, and reaction rates can then be computed from the predicted wave functions using standard relations, preserving the internal consistency of quantum mechanics. This is fundamentally different from directly fitting cross section data, which would yield a purely phenomenological interpolator without access to the underlying wave function.

A central challenge in applying neural networks to scattering wave functions is the energy-dependent oscillation scale. The asymptotic de Broglie wavelength  $\lambda = 2\pi/k$  varies from approximately 9 fm at  $E = 10$  MeV to about 2 fm at  $E = 200$  MeV, a factor of 4.5 variation across the energy range of interest. A network trained on the spatial coordinate  $r$  would need to learn fundamentally different oscillation patterns at different energies: a wave function at 10 MeV completes roughly one oscillation over 9 fm, while at 200 MeV it completes more than four oscillations over the same distance. This makes it extremely difficult for a single network to generalize across energies.

I resolve this challenge by introducing the dimensionless *phase-space coordinate*

$$\rho = kr, \quad (6)$$

where  $k = \sqrt{2\mu E_{\text{cm}}}/\hbar$  is the asymptotic wave number. In  $\rho$ -space, the wavelength is always  $2\pi$  regardless of the projectile energy. This transformation absorbs the energy dependence into the coordinate itself, enabling the network to learn a universal oscillation pattern that applies across all energies. The physical intuition is that  $\rho$  measures distance in units of the de Broglie wavelength, so the wave function always “looks the same” when plotted against  $\rho$ .

For the present calculations, I discretize the radial coordinate into a sequence of 100 points uniformly spaced from  $r = 0.1$  fm to  $r = 15$  fm. At each point, the network receives local information about the potential and physical parameters, and must predict the corresponding wave function value. The sequence of radial points is processed as an ordered sequence, allowing the network to learn how information propagates along the radial direction, analogous to how the Numerov algorithm propagates the solution step by step.

The choice of input features significantly affects the network’s ability to learn and generalize. Raw inputs

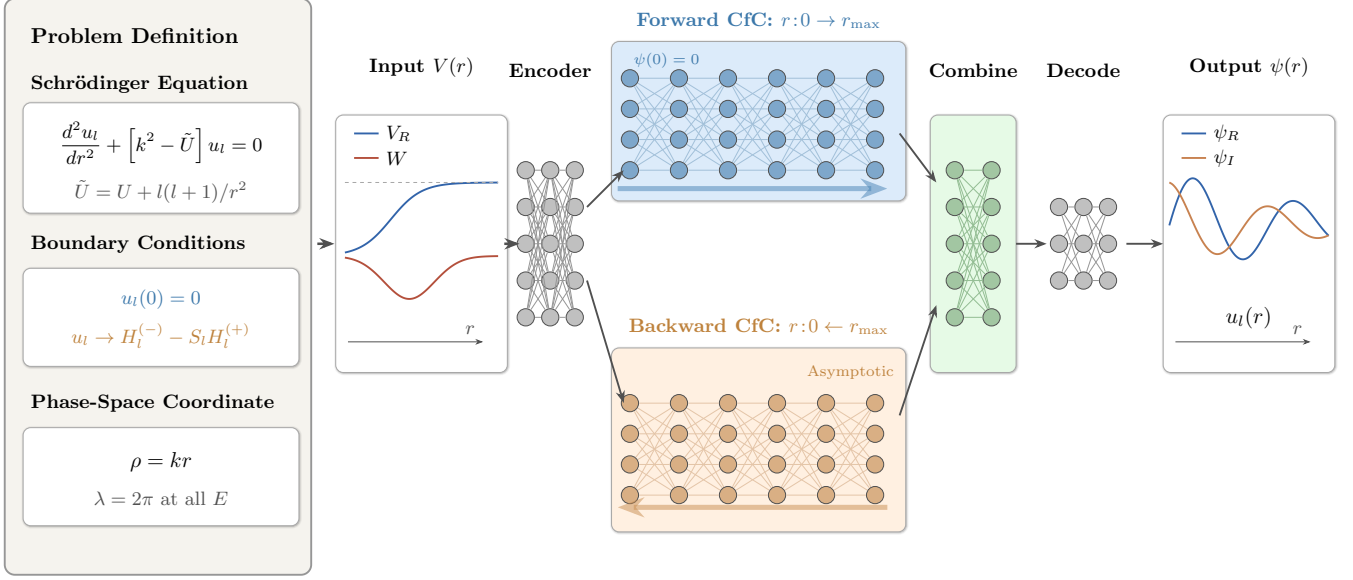


FIG. 1. Schematic of the Bidirectional Liquid Neural Network (BiLNN) architecture for predicting scattering wave functions. **Left panel:** The problem definition, showing the Schrödinger equation with effective potential  $\tilde{U} = U + l(l+1)/r^2$ , the boundary conditions at the origin and at infinity, and the phase-space coordinate transformation  $\rho = kr$ . **Main panel:** The network architecture. The input potential  $V(r)$  and associated features are first processed by an encoder network. The encoded representations feed into two parallel liquid layers: the forward layer integrates from  $r = 0$  toward  $r_{\max}$ , incorporating the boundary condition  $\psi(0) = 0$ , while the backward layer integrates from  $r_{\max}$  toward  $r = 0$ , incorporating asymptotic information. The outputs are concatenated in the combiner, then decoded to produce the real ( $\psi_R$ ) and imaginary ( $\psi_I$ ) parts of the radial wave function  $u_l(r)$ .

such as the potential  $V(r)$  and energy  $E$  span vastly different numerical ranges, which can cause training difficulties. More importantly, the features should encode physically relevant information that helps the network understand the structure of the problem.

At each radial point, the network receives a 9-dimensional feature vector:

$$\mathbf{x} = \left( \frac{\rho}{\rho_{\max}}, \frac{V_R}{E}, \frac{W}{E}, \frac{\eta}{\eta_{\max}}, \sin \phi_{\text{WKB}}, \cos \phi_{\text{WKB}}, D, \frac{l}{l_{\max}}, \frac{A}{A_{\max}} \right). \quad (7)$$

Each feature is designed to capture specific physical information:

- $\rho/\rho_{\max}$ : The normalized phase-space coordinate, ranging from 0 to 1, tells the network “where” along the radial sequence it is currently located.
- $V_R/E$  and  $W/E$ : The real and imaginary parts of the optical potential, normalized by the projectile energy. This ratio determines whether the particle is in a classically allowed ( $V_R < E$ ) or forbidden ( $V_R > E$ ) region, and how strongly absorption affects the wave function at this point.

- $\eta/\eta_{\max}$ : The Sommerfeld parameter  $\eta = Z_1 Z_2 e^2 \mu / (\hbar^2 k)$  characterizes the strength of the Coulomb interaction relative to the kinetic energy. For neutrons,  $\eta = 0$ ; for protons on heavy targets at low energies,  $\eta$  can be substantial.
- $\sin \phi_{\text{WKB}}$  and  $\cos \phi_{\text{WKB}}$ : The WKB phase accumulated from the origin,

$$\phi_{\text{WKB}}(r) = \int_0^r \text{Re}[k_{\text{local}}(r')] dr', \quad (8)$$

where  $k_{\text{local}} = \sqrt{k^2 - 2\mu V(r)/\hbar^2 - l(l+1)/r^2}$  is the local wave number including the centrifugal barrier. Providing both sine and cosine avoids the discontinuity at  $\phi = 2\pi$  and gives the network direct information about the expected oscillation phase.

- $D$ : The WKB decay factor, computed as  $D = \exp(-\int_0^r \text{Im}[k_{\text{local}}] dr')$ , captures the cumulative absorption due to the imaginary potential. This helps the network predict the amplitude envelope of the wave function.
- $l/l_{\max}$  and  $A/A_{\max}$ : The normalized partial wave quantum number and target mass number encode the discrete parameters of the problem.

All features are normalized to lie approximately in the range  $[0, 1]$  or  $[-1, 1]$ , which improves numerical stability during optimization. The WKB-based features ( $\phi_{\text{WKB}}$  and  $D$ ) provide semiclassical guidance that significantly improves the network’s ability to capture the oscillatory structure and absorption effects.

A basic neural network treats each radial point independently, with no mechanism to propagate information along the radial coordinate. However, the Schrödinger equation is a differential equation where the wave function at each point depends on its values at neighboring points, since the solution at  $r$  is determined by “integrating” from the boundary. To capture this sequential structure, I use a *recurrent* architecture that processes the radial grid points in order, maintaining an internal state  $\mathbf{h}$  that accumulates information as it steps through the sequence:

$$\mathbf{h}_n = f(\mathbf{h}_{n-1}, \mathbf{x}_n), \quad (9)$$

where  $n$  indexes the radial grid points and  $f$  is a learned update function. This is directly analogous to how the Numerov algorithm propagates the solution from  $r = 0$  outward, except that the propagation rule is learned from data rather than derived from a finite-difference approximation.

The choice of recurrent architecture requires careful consideration. Standard recurrent networks such as Long Short-Term Memory (LSTM) [18] suffer from gradient degradation when processing long sequences, a significant limitation given that the radial grids contain 100 points and may need to be extended for heavy nuclei or higher energies. More fundamentally, the discrete gating mechanisms in LSTM are not naturally suited to problems governed by continuous differential equations.

I therefore employ *Liquid Neural Networks* [16], whose internal dynamics are themselves described by differential equations. This choice provides a crucial *inductive bias*: rather than learning arbitrary sequence-to-sequence mappings, the network is constrained to evolve its hidden state according to a learnable ordinary differential equation, structurally aligned with the Schrödinger equation I seek to emulate. Originally developed for *temporal* sequences, these Closed-form Continuous-time (CfC) layers model the hidden state evolution as a first-order ODE with learnable time constants and nonlinear driving terms. Crucially, the ODE admits closed-form analytical solutions, providing both computational efficiency and stable gradient propagation during training.

A key innovation of the present work is the reinterpretation of liquid networks from *temporal* to *spatial* dynamics. The time variable is replaced with the radial coordinate  $r$ , transforming the network into a *spatial* propagator:

$$\frac{d\mathbf{h}}{dr} = -\frac{\mathbf{h}}{\lambda} + \mathbf{g}(\mathbf{h}, \mathbf{x}), \quad (10)$$

where  $\lambda$  now represents a learnable “relaxation length” rather than a time constant. This reinterpretation is natural for the scattering problem: just as the original CfC

layers learn to propagate information forward in time, the spatial liquid layers learn to propagate the wave function solution along the radial coordinate, in a manner directly analogous to numerical integration of the Schrödinger equation.

The scattering Schrödinger equation is a *boundary value problem* with conditions specified at both ends of the domain:  $u_l(0) = 0$  at the origin and the asymptotic Coulomb behavior  $u_l \rightarrow H_l^{(-)} - S_l H_l^{(+)}$  as  $r \rightarrow \infty$ . A unidirectional network that processes only from small to large  $r$  naturally incorporates information about the left boundary condition but has no direct knowledge of the right boundary condition, since it can only “see” what came before, not what comes after.

To incorporate both boundary conditions, I employ a *bidirectional* architecture with two parallel networks. The **forward** network processes the radial sequence from  $r = 0$  to  $r_{\text{max}}$ , propagating information about the boundary condition  $u_l(0) = 0$  outward. The **backward** network processes the sequence in reverse, from  $r_{\text{max}}$  to  $r = 0$ , propagating information about the asymptotic behavior inward. At each radial point, the outputs from both directions are combined to form a representation that incorporates information from both boundaries. This bidirectional processing is analogous to the shooting method in numerical analysis, where solutions are propagated from both boundaries and matched in the middle.

The complete BiLNN architecture consists of five components (see Fig. 1): (i) an **encoder** that transforms the 9-dimensional input features into a higher-dimensional internal representation suitable for processing; (ii) the **forward liquid** layer that processes this representation from  $r = 0$  outward; (iii) the **backward liquid** layer that processes in reverse from  $r_{\text{max}}$  inward; (iv) a **combiner** that merges the forward and backward information at each radial point; and (v) a **decoder** that transforms the internal representation back into the physical output ( $\psi_R, \psi_I$ ). The liquid layers use a structured sparse connectivity [19] with 128 internal units each.

The total model has approximately 1.2 million adjustable parameters. While this may seem large, these parameters are determined once during training and then fixed. The trained network can evaluate wave functions for any combination of inputs within its training domain essentially instantaneously, since the computational cost of solving the differential equation has been amortized into the one-time training process.

Training data is generated by solving Eq. (1) numerically using the Numerov method for random combinations of physical parameters. The training set covers:

- Twelve target nuclei:  $^{12}\text{C}$ ,  $^{16}\text{O}$ ,  $^{27}\text{Al}$ ,  $^{28}\text{Si}$ ,  $^{40}\text{Ca}$ ,  $^{48}\text{Ti}$ ,  $^{56}\text{Fe}$ ,  $^{58}\text{Ni}$ ,  $^{90}\text{Zr}$ ,  $^{120}\text{Sn}$ ,  $^{197}\text{Au}$ , and  $^{208}\text{Pb}$ , spanning the periodic table from light to heavy nuclei.
- Both projectile types: protons and neutrons.
- Energies uniformly sampled from 1 to 200 MeV.

- Partial waves from  $l = 0$  to  $l = 30$ , sufficient to converge the cross section at all energies considered.

For each combination of target and projectile type, I generate 100 random energy samples for each partial wave, yielding approximately 74,400 training examples in total. The wave functions are normalized by their maximum absolute value to bring all samples to a comparable scale. Each wave function is evaluated on the uniform grid of 100 radial points.

The dataset is split into 80% for training and 20% for testing. The test set is used to evaluate generalization performance on parameter combinations not seen during training. Importantly, the test set includes interpolation within the training domain (e.g., an energy of 75 MeV when trained on samples at 70 and 80 MeV) rather than extrapolation beyond it.

The cost function to be minimized is the mean squared error between predicted and true wave functions, where  $\psi_R$  and  $\psi_I$  denote the real and imaginary parts of the complex wave function  $u_l(r)$ :

$$\mathcal{L} = \frac{1}{N} \sum_{i=1}^N \left[ (\psi_R^{\text{pred}} - \psi_R^{\text{true}})^2 + (\psi_I^{\text{pred}} - \psi_I^{\text{true}})^2 \right], \quad (11)$$

where the sum runs over all radial points in all training samples. This treats the real and imaginary parts equally and penalizes deviations at all radii uniformly.

The optimization is performed using the AdamW algorithm [20] over 500 iterations through the training data (epochs), with the step size gradually reduced as the solution converges. A small regularization term is added to prevent overfitting to the training data. On a modern GPU, training completes in approximately 3–4 hours.

#### IV. RESULTS

The trained BiLNN is evaluated on a held-out test set comprising 20% of the total data (approximately 14,880 samples), with parameter combinations not seen during training. The overall relative error, defined as the root-mean-square deviation between predicted and true wave functions normalized by the wave function amplitude, is 1.2% averaged over all test samples. This level of accuracy is sufficient for most practical applications, as it corresponds to errors in the scattering  $S$ -matrix of comparable magnitude.

Figure 2 presents a detailed comparison of wave functions predicted by BiLNN with numerically exact Numerov solutions for four representative test cases that span different projectile types, target nuclei, energies, and partial waves. Panel (a) shows the  $s$ -wave ( $l = 0$ ) radial wave function for proton scattering on  $^{208}\text{Pb}$  at  $E = 83$  MeV, where the real part exhibits approximately 5 complete oscillations within the radial range  $r = 0$ –15 fm, with amplitude growing from small values near

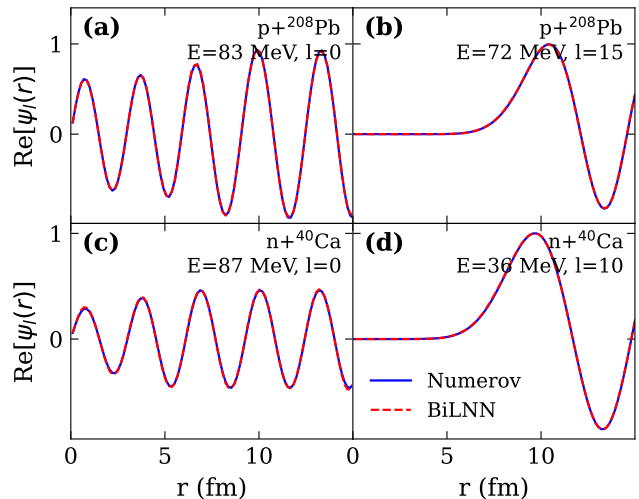


FIG. 2. Comparison of wave functions predicted by BiLNN (dashed red lines) with numerically exact Numerov solutions (solid blue lines) for representative test cases. (a)  $p+^{208}\text{Pb}$  at  $E = 83$  MeV,  $l = 0$ :  $s$ -wave showing full penetration to the nuclear interior with  $\sim 5$  oscillations; (b)  $p+^{208}\text{Pb}$  at  $E = 72$  MeV,  $l = 15$ : high- $l$  partial wave with centrifugal barrier suppression at small  $r$ ; (c)  $n+^{40}\text{Ca}$  at  $E = 87$  MeV,  $l = 0$ : neutron  $s$ -wave without Coulomb effects; (d)  $n+^{40}\text{Ca}$  at  $E = 36$  MeV,  $l = 10$ : lower-energy neutron with centrifugal suppression. The network accurately reproduces both amplitude and phase across all cases.

the origin (where the strong nuclear and Coulomb potentials suppress the wave function) to maximum amplitude around  $r \approx 8$  fm before settling into the asymptotic Coulomb behavior. The BiLNN prediction (dashed red) overlays the Numerov reference (solid blue) with deviations barely visible on this scale, demonstrating sub-percent accuracy in both amplitude and phase. Panel (b) displays the  $l = 15$  partial wave for the same  $p+^{208}\text{Pb}$  system at  $E = 72$  MeV. Here the centrifugal barrier  $l(l+1)/r^2$  creates a classically forbidden region at small radii, suppressing the wave function to nearly zero for  $r \lesssim 5$  fm. Beyond the classical turning point, the wave function emerges with oscillatory behavior confined to the exterior region  $r > 5$  fm. The network accurately captures both the exponential suppression in the forbidden region and the subsequent oscillatory structure, including the correct phase at the matching radius. Panels (c) and (d) show neutron scattering on  $^{40}\text{Ca}$ , where the absence of Coulomb interaction simplifies the potential but the wave function must still satisfy the correct asymptotic matching to spherical Bessel functions. At  $E = 87$  MeV [panel (c),  $l = 0$ ], the  $s$ -wave penetrates to the origin and shows approximately 5 oscillations with the characteristic pattern of increasing amplitude toward the asymptotic region. At  $E = 36$  MeV [panel (d),  $l = 10$ ], the lower energy combined with the centrifugal barrier produces a wave function that is suppressed for  $r \lesssim 4$  fm and exhibits only a single oscillation in

the exterior region, with longer wavelength reflecting the lower kinetic energy. In all cases, the phase agreement between BiLNN and Numerov is excellent across the entire radial range, demonstrating that the phase-space coordinate representation successfully enables generalization across the wide energy range.

Since the ultimate goal of optical model calculations is to predict scattering observables, I verify that the wave function accuracy translates to accurate  $S$ -matrix elements and cross sections. The  $S$ -matrix is extracted from the predicted wave functions using the amplitude integral method [4]

$$f_l = -\frac{1}{E} \int_0^\infty F_l(\eta, kr) V(r) \psi_l(r) dr, \quad (12)$$

where  $F_l$  is the regular Coulomb function, giving  $S_l = 1 + 2ikf_l$ . This integral formulation is preferred over asymptotic matching because it weights the wave function by the potential, making it less sensitive to errors in the asymptotic region where the wave function amplitude is large but the physical information content is low.

Figure 3 compares the  $S$ -matrix modulus  $|S_l|$  and phase  $\arg(S_l)$  obtained from BiLNN and Numerov wave functions for proton scattering on  $^{208}\text{Pb}$  at three representative energies: 27 MeV (left column), 83 MeV (center column), and 157 MeV (right column). The top row [panels (a)–(c)] displays  $|S_l|$  as a function of partial wave  $l$ . At the lowest energy  $E = 27$  MeV [panel (a)], the  $S$ -matrix modulus shows a complex oscillatory pattern at low  $l$ , with  $|S_l|$  varying between 0.4 and 0.75 for  $l \lesssim 10$ , reflecting interference between nuclear and Coulomb amplitudes in this strongly absorbing regime. Beyond  $l \approx 12$ , the transition to transparency ( $|S_l| \approx 1$ ) is sharp, occurring over just 2–3 partial waves. At intermediate energy  $E = 83$  MeV [panel (b)], the absorption region extends to higher partial waves ( $l \lesssim 14$ ), with  $|S_l|$  showing similar oscillatory structure in the interior region before the sharp rise to unity. At the highest energy  $E = 157$  MeV [panel (c)], the grazing angular momentum shifts further to  $l_g \approx 20$ , and the oscillatory pattern in  $|S_l|$  becomes more pronounced, with values dropping as low as 0.3 before recovering. This energy-dependent shift of the absorption edge reflects the increasing classical impact parameter  $b = l/k$  at higher energies, with the grazing condition  $b \approx R$  determining where the projectile trajectory begins to miss the nuclear volume. The BiLNN predictions (red squares) overlay the Numerov reference values (blue circles) with excellent agreement across all partial waves, accurately capturing the oscillatory structure, absorption depth, and transition sharpness. The bottom row [panels (d)–(f)] shows the  $S$ -matrix phase  $\arg(S_l)$ , which encodes the combined nuclear and Coulomb phase shifts. At low energies [panel (d)], the phase exhibits rapid variation with  $l$ , starting near +2 radians at  $l = 0$  and dropping sharply to  $-2$  radians around  $l \approx 6$  before recovering to zero at high  $l$ . At higher energies [panels (e) and (f)], the phase variation becomes smoother but extends to higher  $l$  values before asymptoting to zero.

The network reproduces these phase patterns with high fidelity, which is crucial since even small phase errors would produce significant deviations in the interference patterns of the cross section.

The elastic scattering cross section is the experimentally observable quantity that tests whether the coherent sum over partial waves preserves the accuracy of the individual  $S$ -matrix elements. Figure 4 shows the proton elastic scattering angular distribution expressed as the ratio to Rutherford scattering,  $d\sigma/d\sigma_{\text{Ruth}}$ , for three target nuclei at two energies each:  $^{40}\text{Ca}$  [panels (a) and (d)],  $^{90}\text{Zr}$  [panels (b) and (e)], and  $^{208}\text{Pb}$  [panels (c) and (f)]. The top row shows lower-energy cases, while the bottom row shows higher-energy cases. In all cases, the BiLNN predictions (red dashed lines) faithfully reproduce both the positions and depths of the diffraction minima.

For neutron scattering, where no Coulomb interaction is present, Figure 5 displays the differential cross section  $d\sigma/d\Omega$  in mb/sr for six target nuclei:  $^{12}\text{C}$  [panel (a)],  $^{40}\text{Ca}$  [panel (b)],  $^{90}\text{Zr}$  [panel (c)],  $^{56}\text{Fe}$  [panel (d)],  $^{120}\text{Sn}$  [panel (e)], and  $^{208}\text{Pb}$  [panel (f)]. The absence of the Coulomb amplitude eliminates the Rutherford divergence at forward angles. In all cases, the BiLNN predictions capture both the overall magnitude and the detailed oscillatory structure.

Figure 6 provides a comprehensive summary of the error distribution across the parameter space, restricted to physically contributing partial waves satisfying  $l < kR + 5$  where  $R \approx 1.2A^{1/3}$  fm. This criterion excludes high- $l$  partial waves for light nuclei at low energies, where the centrifugal barrier prevents the wave function from penetrating into the nuclear interior and therefore makes negligible contribution to the cross section. Panel (a) displays the relative error as a function of partial wave quantum number  $l$ . The error shows a non-monotonic dependence on angular momentum: both low- $l$  partial waves ( $l \lesssim 4$ ) and high- $l$  partial waves ( $l \gtrsim 24$ ) exhibit errors of approximately 1.5–1.8%, while intermediate partial waves ( $l \approx 8$ –16) achieve the lowest errors around 1.0%. The elevated error at low  $l$  can be understood physically: for  $s$ -waves and low partial waves, the wave function penetrates deep into the nuclear interior where both the nuclear attraction and Coulomb repulsion (for protons) are strongest, requiring the network to capture rapid variations in a region of steep potential gradients. The slightly elevated error at high  $l$  may reflect the increased sensitivity to the asymptotic matching region, where small phase errors accumulate over many oscillations. Panel (b) shows the error breakdown by target nucleus for all twelve nuclei in the training set. The errors are uniform for light and medium-mass nuclei from  $^{12}\text{C}$  to  $^{120}\text{Sn}$ , clustering around 0.8–1.3%, while the heaviest targets  $^{197}\text{Au}$  and  $^{208}\text{Pb}$  show somewhat larger errors of 1.6–1.8%. This trend can be attributed to the stronger Coulomb interaction for proton scattering on heavy targets, which introduces additional oscillatory structure at large distances and requires more extended matching radii. The horizontal dashed line indicates the

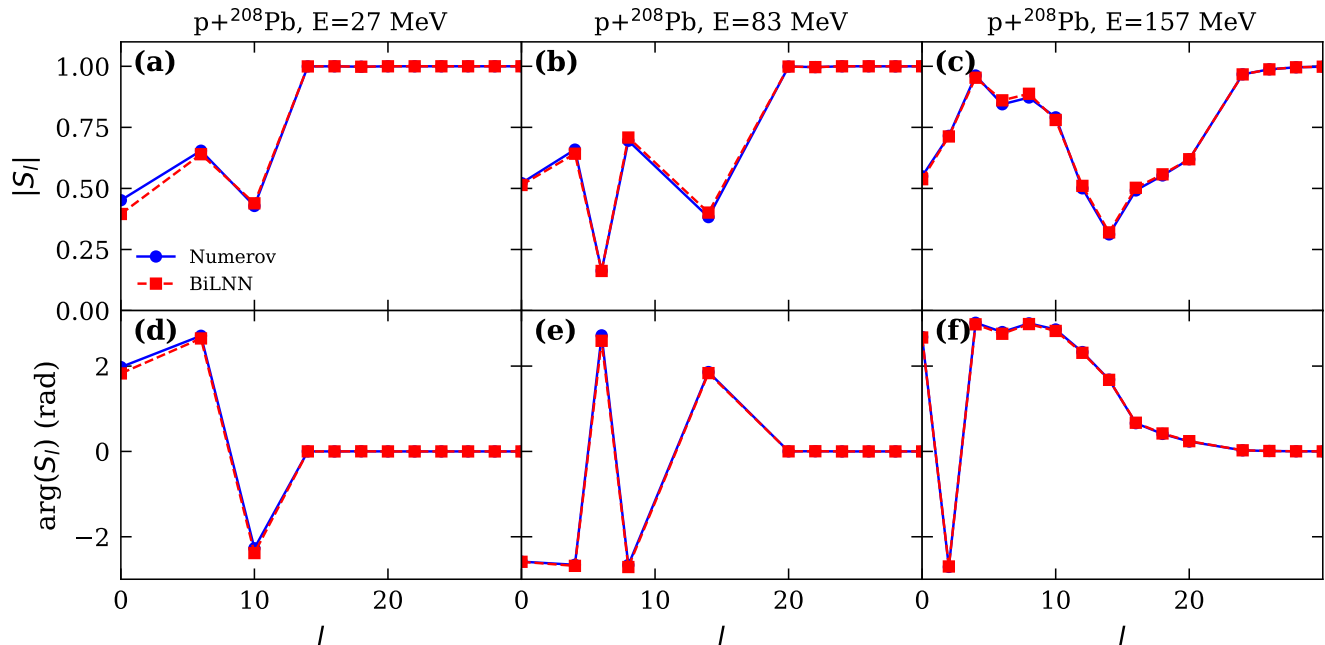


FIG. 3.  $S$ -matrix comparison for  $p+^{208}\text{Pb}$  scattering at three energies:  $E = 27$  MeV (left),  $E = 83$  MeV (center), and  $E = 157$  MeV (right). Top row [(a)–(c)]:  $|S_l|$  showing oscillatory absorption at low  $l$  with sharp transition to transparency ( $|S_l| \rightarrow 1$ ) at the grazing angular momentum  $l_g$ , which increases with energy from  $l_g \approx 12$  at 27 MeV to  $l_g \approx 20$  at 157 MeV. Bottom row [(d)–(f)]:  $\arg(S_l)$  showing the nuclear and Coulomb phase shifts, with rapid  $l$ -dependence at low energies that smooths out at higher energies. Blue circles: Numerov reference; red squares: BiLNN prediction.

overall average error of 1.2%. Panel (c) reveals the most pronounced systematic dependence: the error varies significantly with projectile energy, from approximately 4% at the lowest energies (1–20 MeV) down to about 1% at high energies (above 100 MeV). This trend reflects the challenge of learning wave functions at low energies where the de Broglie wavelength is longest: the wave function exhibits fewer oscillations within the nuclear interior, providing less structure for the network to learn, and the relative phase error has larger impact on the overall solution. At higher energies, the more rapid oscillations are well captured by the phase-space coordinate representation, resulting in errors close to or below the overall average.

A key test of whether the network has learned the underlying physics rather than merely memorizing the training data is its ability to extrapolate to nuclei not included in training. Figure 7 shows predictions for three nuclei that were never seen during training:  $^{24}\text{Mg}$  ( $A = 24$ ,  $Z = 12$ ),  $^{63}\text{Cu}$  ( $A = 63$ ,  $Z = 29$ ), and  $^{184}\text{W}$  ( $A = 184$ ,  $Z = 74$ ). These targets were deliberately chosen to lie between the training nuclei in atomic mass:  $^{24}\text{Mg}$  between  $^{16}\text{O}$  and  $^{27}\text{Al}$ ,  $^{63}\text{Cu}$  between  $^{58}\text{Ni}$  and  $^{90}\text{Zr}$ , and  $^{184}\text{W}$  between  $^{120}\text{Sn}$  and  $^{197}\text{Au}$ , testing interpolation capability with nuclei having different proton-to-neutron ratios that affect the optical potential parameters through the isospin dependence of the KD02 parameterization. The top row [panels (a)–(c)] displays  $s$ -wave

( $l = 0$ ) proton scattering wave functions at intermediate energies. For  $^{24}\text{Mg}$  at  $E = 76$  MeV [panel (a)], the light target produces a wave function with approximately 4 oscillations and relatively uniform amplitude, characteristic of weak absorption in the small nuclear volume. For  $^{63}\text{Cu}$  at  $E = 88$  MeV [panel (b)], the larger nuclear radius shifts the oscillatory pattern outward with approximately 5 oscillations visible, while the wave function amplitude grows more pronounced toward the asymptotic region. For  $^{184}\text{W}$  at  $E = 38$  MeV [panel (c)], the combination of heavy target and lower energy produces a wave function with fewer oscillations (longer wavelength) but still excellent agreement between BiLNN and Numerov across the full radial range. The bottom row [panels (d)–(f)] shows the corresponding elastic scattering cross sections  $d\sigma/d\sigma_{\text{Ruth}}$ . For  $^{24}\text{Mg}$  [panel (d)], the cross section ratio remains above unity across most angles with a single broad minimum. For  $^{63}\text{Cu}$  [panel (e)], multiple diffraction minima appear spanning nearly four orders of magnitude in cross section ratio. For  $^{184}\text{W}$  [panel (f)], the strong Coulomb field produces a pattern with the ratio declining smoothly from forward angles to backward angles. In all cases, the BiLNN predictions closely track the Numerov reference, demonstrating that the network has learned the smooth dependence of the scattering solution on atomic mass  $A$  and charge  $Z$  embedded in the optical potential, rather than memorizing target-specific patterns.

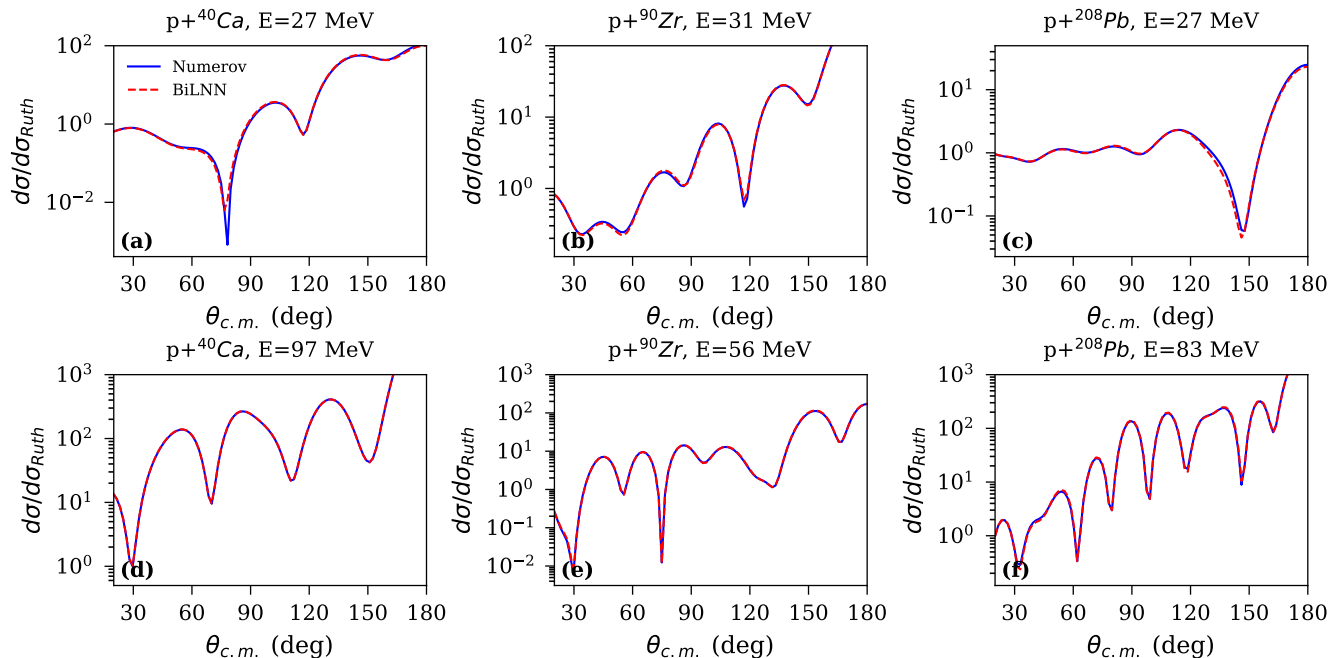


FIG. 4. Proton elastic scattering angular distributions  $d\sigma/d\sigma_{\text{Ruth}}$  for three target nuclei at two energies each. (a,d)  $^{40}\text{Ca}$  at  $E = 27$  MeV and  $E = 97$  MeV; (b,e)  $^{90}\text{Zr}$  at  $E = 31$  MeV and  $E = 56$  MeV; (c,f)  $^{208}\text{Pb}$  at  $E = 27$  MeV and  $E = 83$  MeV. The top row shows lower-energy cases with broader diffraction features; the bottom row shows higher-energy cases with more compressed, sharper minima. Blue solid lines: Numerov reference; red dashed lines: BiLNN prediction. The diffraction patterns, including positions, depths, and widths of multiple minima, are reproduced across up to four orders of magnitude in cross section ratio.

The bidirectional architecture proves essential for achieving this level of accuracy. I compared the BiLNN with a unidirectional variant that processes the radial sequence only in the forward direction (from  $r = 0$  outward). On the same training data, the unidirectional network achieved a relative error of 1.4%, compared to 1.2% for the bidirectional version, a 14% reduction in error. The improvement is most pronounced for higher partial waves and near the matching radius, where the backward pass provides direct information about the asymptotic boundary condition that propagates inward to constrain the interior solution.

The primary advantage of the neural network approach is not computational speed, but *differentiability*. The Numerov algorithm, while highly efficient for forward calculations, is fundamentally opaque to gradient-based optimization: computing the derivative of observables with respect to potential parameters requires either finite-difference approximations (which scale poorly with parameter dimensionality) or algorithmic differentiation of the entire integration loop (which is technically challenging and rarely implemented). In contrast, the trained BiLNN provides gradients “for free” through automatic differentiation, with computational cost comparable to the forward pass. This enables gradient-based approaches to inverse problems, such as direct optimization of optical model parameters against experimental

data and efficient exploration of parameter uncertainties via Hamiltonian Monte Carlo or other gradient-informed sampling methods. For applications where millions of gradient evaluations are required, such as Bayesian inference over high-dimensional parameter spaces, the differentiable surrogate offers a qualitative advantage that transcends simple speedup factors.

## V. CONCLUSIONS

I have developed a neural network emulator for nucleon-nucleus scattering wave functions based on a Bidirectional Liquid Neural Network (BiLNN) architecture. The central motivation is not merely computational speedup, but the construction of a *differentiable* mapping from optical potential parameters to scattering wave functions, enabling gradient-based approaches to inverse problems that are inaccessible with traditional numerical integrators. This work establishes a proof of concept for two key methodological innovations that make such a differentiable solver practical: (i) the phase-space coordinate  $\rho = kr$ , which normalizes the oscillation wavelength regardless of projectile energy, and (ii) the BiLNN architecture, which naturally incorporates boundary conditions at both ends of the domain. Together, these advances enable a single network to generalize across the

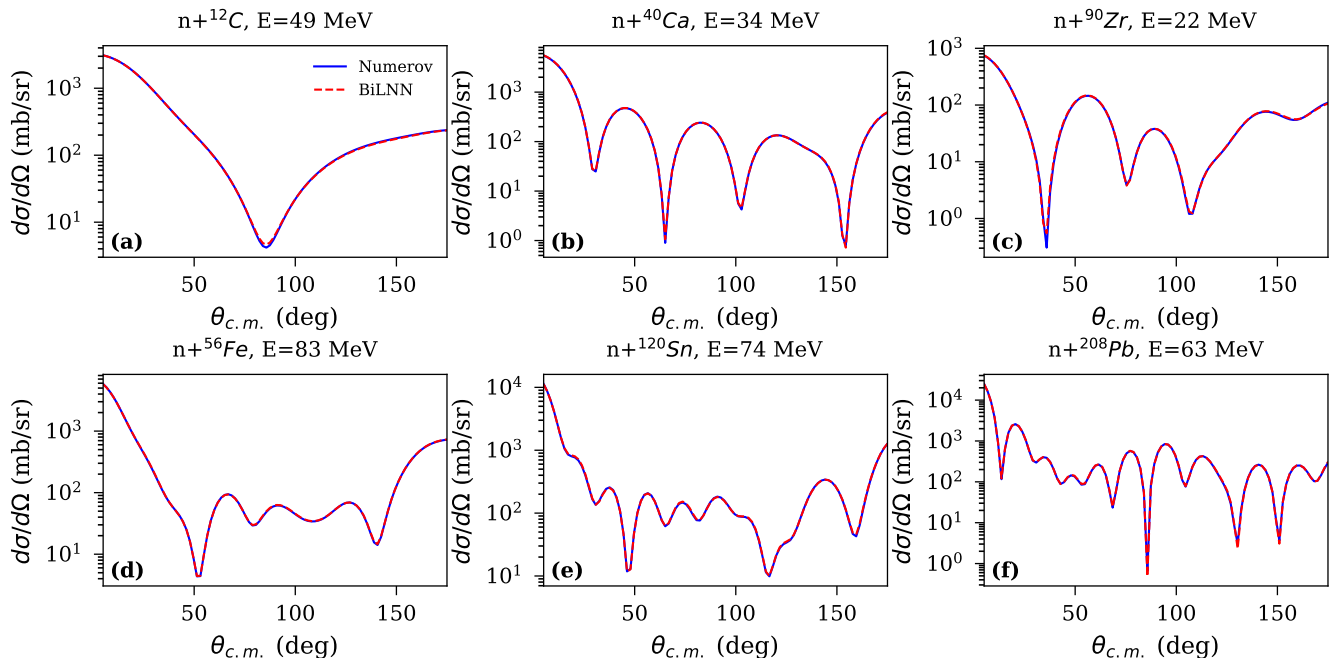


FIG. 5. Neutron elastic scattering angular distributions  $d\sigma/d\Omega$  for six target nuclei spanning the training set. (a)  $^{12}\text{C}$  at  $E = 49$  MeV; (b)  $^{40}\text{Ca}$  at  $E = 34$  MeV; (c)  $^{90}\text{Zr}$  at  $E = 22$  MeV; (d)  $^{56}\text{Fe}$  at  $E = 83$  MeV; (e)  $^{120}\text{Sn}$  at  $E = 74$  MeV; (f)  $^{208}\text{Pb}$  at  $E = 63$  MeV. Blue solid lines: Numerov reference; red dashed lines: BiLNN prediction.

wide parameter space, achieving a relative error of 1.2% across twelve target nuclei from  $^{12}\text{C}$  to  $^{208}\text{Pb}$ , both proton and neutron projectiles, energies from 1 to 200 MeV, and partial waves up to  $l = 30$ .

A fundamental aspect of this approach is that I learn the wave function itself rather than directly predicting observables such as cross sections or  $S$ -matrix elements. The wave function is the most fundamental quantum mechanical object in scattering theory, encoding the complete information about the collision process. From a single predicted wave function, one can extract phase shifts,  $S$ -matrix elements, elastic and reaction cross sections, and any other scattering observable, all while preserving the internal consistency of quantum mechanics. This is in contrast to approaches that directly fit observables, which would require separate models for each quantity and offer no access to the underlying quantum state.

The wave function accuracy translates directly to accurate scattering observables. The  $S$ -matrix elements extracted from the predicted wave functions reproduce both the absorption pattern ( $|S_l|$ ) and phase shifts across all partial waves. The resulting elastic scattering angular distributions,  $d\sigma/d\sigma_{\text{Ruth}}$  for protons and  $d\sigma/d\Omega$  for neutrons, match the Numerov reference calculations within a few percent, capturing diffraction patterns spanning more than four orders of magnitude. Importantly, the network extrapolates successfully to nuclei not included in training ( $^{24}\text{Mg}$ ,  $^{63}\text{Cu}$ ,  $^{184}\text{W}$ ), with errors comparable to in-sample predictions. This demonstrates that the model has learned the physics encoded in the optical po-

tential rather than memorizing target-specific patterns.

The success of this approach offers several physical insights. First, the effectiveness of the phase-space coordinate  $\rho = kr$  reveals that scattering wave functions possess a universal structure when viewed in the natural units of the de Broglie wavelength. This is a direct manifestation of the scale invariance inherent in quantum mechanics: the oscillatory behavior of the wave function is determined by the ratio of the local momentum to the asymptotic momentum, not by absolute length scales. The network exploits this universality to generalize across a factor of 4.5 in energy with a single set of parameters.

Second, the successful extrapolation to nuclei outside the training set ( $^{24}\text{Mg}$ ,  $^{63}\text{Cu}$ ,  $^{184}\text{W}$ ) provides evidence that the global optical model contains a deeper universality than might be apparent from its empirical parameterization. The network has evidently learned the smooth dependence of the potential on mass number  $A$  and the resulting systematic trends in wave function behavior, suggesting that the KD02 parameterization captures genuine physical regularities rather than merely fitting isolated data points.

Third, the inclusion of WKB phase and absorption factors as input features demonstrates how semiclassical physics can guide machine learning. These features encode the leading-order behavior expected from the correspondence principle, allowing the network to focus on learning the quantum corrections. This hierarchical approach, where classical or semiclassical physics provides the backbone and machine learning captures the residual

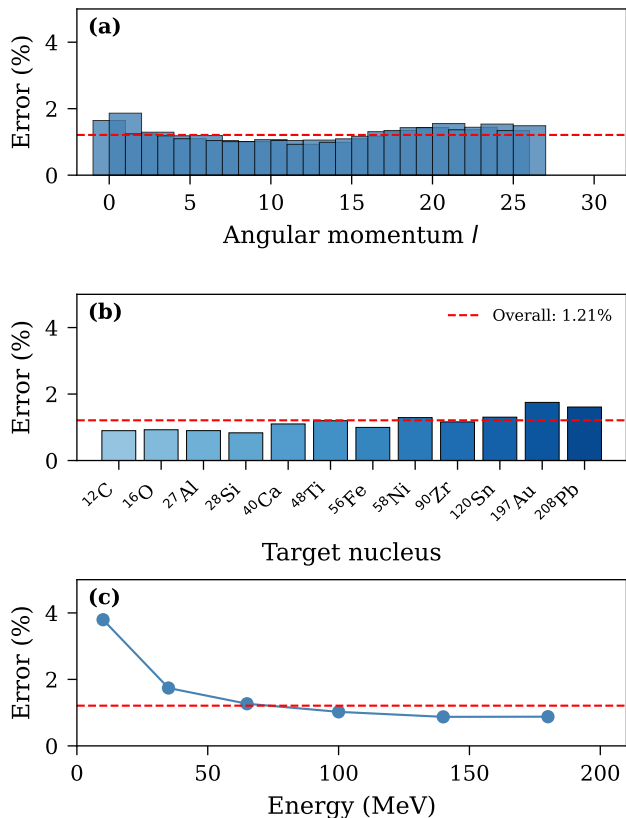


FIG. 6. Summary of neural network prediction errors for physically contributing partial waves ( $l < kR + 5$ , where  $R \approx 1.2A^{1/3}$  fm). (a) Error versus partial wave  $l$ , showing elevated errors ( $\sim 1.5$ – $1.8\%$ ) at both low  $l$  (deep nuclear penetration) and high  $l$  (asymptotic sensitivity), with minimum errors ( $\sim 1\%$ ) at intermediate  $l \approx 8$ – $16$ ; (b) Error by target nucleus for all twelve training targets, with uniform accuracy ( $0.8$ – $1.3\%$ ) for light-to-medium nuclei and slightly higher errors ( $1.6$ – $1.8\%$ ) for the heaviest targets; (c) Error versus projectile energy, showing the strongest systematic dependence:  $\sim 4\%$  at low energies ( $1$ – $20$  MeV) decreasing to  $\sim 1\%$  above  $100$  MeV. The dashed lines indicate the overall average error of  $1.2\%$ .

quantum effects, may prove broadly applicable to other problems at the interface of classical and quantum mechanics.

More broadly, this work demonstrates the potential of combining neural network architectures with physics-guided input representations and domain-specific coordinate transformations to solve quantum mechanical scattering problems. Unlike physics-informed neural networks (PINNs) that encode differential equations directly

in the loss function, this approach incorporates physical knowledge through the design of input features (phase-space coordinates, WKB phases) and network architecture (bidirectional structure matching boundary conditions). This physics-guided surrogate modeling approach offers a promising paradigm for machine learning applications in nuclear physics.

Although the present calculation omits the spin-orbit interaction for simplicity, the extension is mathematically straightforward. Including spin-orbit coupling adds an additional surface-derivative term to the potential, and for each partial wave  $l > 0$  requires solving two separate single-channel equations for  $j = l \pm 1/2$ . This can be accommodated by including the total angular momentum  $j$  as an additional input feature to the network. The success of the BiLNN architecture in handling oscillatory wave functions with complex boundary conditions, as demonstrated here, provides confidence that this extension will preserve the accuracy and generalization capability. The same principle applies to coupled-channel calculations involving inelastic excitations, where each channel contributes an additional component to the wave function vector. This scalability to multi-channel problems, where the computational advantage of neural network surrogates becomes more pronounced, is the immediate next step toward practical nuclear data evaluation applications.

The trained model provides a fully differentiable surrogate for the scattering Schrödinger equation. Unlike the Numerov algorithm, which is opaque to gradient-based optimizers, the neural network allows gradients of any observable (cross sections, phase shifts, reaction rates) to flow back to the optical potential parameters through automatic differentiation. This capability opens the door to end-to-end optimization of optical model parameters against experimental data, efficient exploration of parameter uncertainties via gradient-informed sampling, and seamless integration into larger differentiable physics pipelines. The present work establishes the foundational architecture; exploiting its differentiability for inverse problems in nuclear data evaluation is the subject of ongoing investigation.

## ACKNOWLEDGMENTS

This work was supported by the National Natural Science Foundation of China (Grant Nos. 12475132 and 12535009) and the Fundamental Research Funds for the Central Universities.

[1] P. E. Hodgson, *Nuclear Reactions and Nuclear Structure* (Clarendon Press, Oxford, 1971).  
 [2] G. R. Satchler, *Direct Nuclear Reactions* (Oxford Uni-

versity Press, Oxford, 1983).

[3] A. J. Koning and J. P. Delaroche, *Nucl. Phys. A* **713**, 231 (2003).

## Extrapolation: Nuclei NOT in Training Set

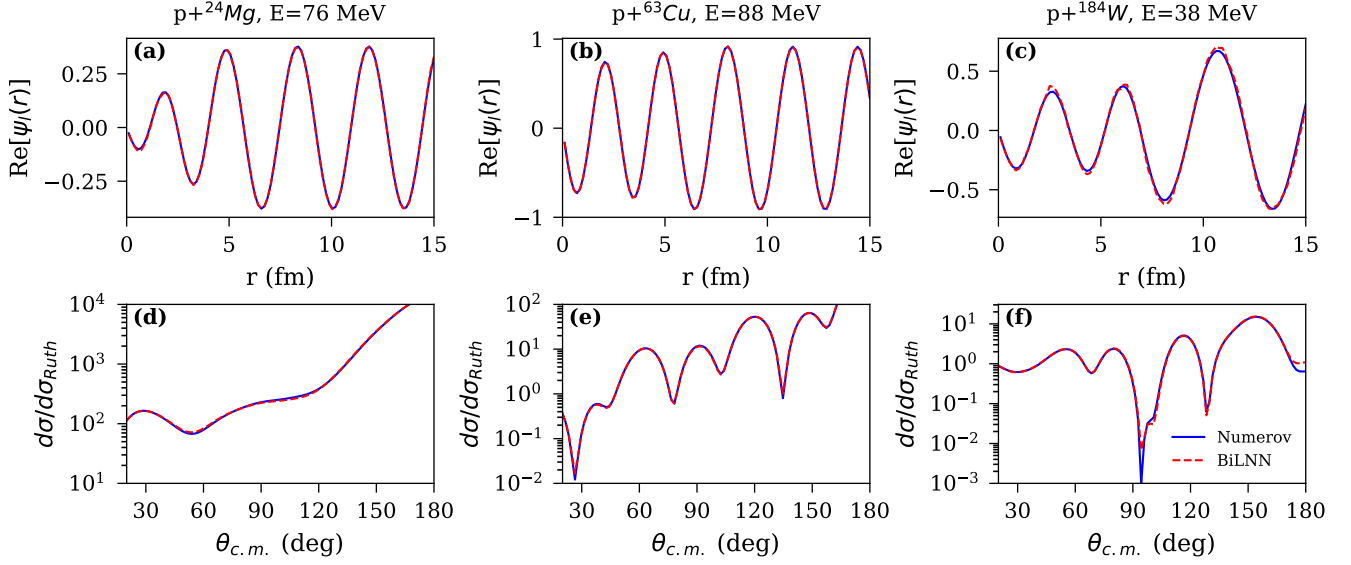


FIG. 7. Extrapolation test for nuclei *not* included in training:  $^{24}\text{Mg}$  (left),  $^{63}\text{Cu}$  (center), and  $^{184}\text{W}$  (right). Top row [(a)–(c)]:  $s$ -wave proton wave functions at  $E = 76$ ,  $88$ , and  $38$  MeV, respectively, showing the real part of  $\psi_l(r)$ ; bottom row [(d)–(f)]: corresponding elastic scattering cross sections  $d\sigma/d\sigma_{\text{Ruth}}$  spanning up to four orders of magnitude. Blue: Numerov reference; red: BiLNN prediction. The network generalizes successfully to these unseen nuclei with accuracy comparable to the training set, demonstrating that it has learned the physics of the optical model rather than memorizing target-specific patterns.

- [4] I. J. Thompson and F. M. Nunes, *Nuclear Reactions for Astrophysics* (Cambridge University Press, Cambridge, 2009).
- [5] T. Aumann, C. A. Bertulani, and J. Ryckebusch, *Phys. Rev. C* **88**, 064610 (2013).
- [6] C. Hebborn, F. M. Nunes, G. Potel, W. H. Dickhoff, J. W. Holt, M. C. Atkinson, R. B. Baker, C. Barbieri, G. Blanchon, M. Burrows, R. Capote, P. Danielewicz, M. Dupuis, C. Elster, J. E. Escher, L. Hlophe, A. Idini, H. Jayatissa, B. P. Kay, K. Kravvaris, J. J. Manfredi, A. Mercenne, B. Morillon, G. Perdikakis, C. D. Pruitt, G. H. Sargsyan, I. J. Thompson, M. Vorabbi, and T. R. Whitehead, *Journal of Physics G: Nuclear and Particle Physics* **50**, 060501 (2023).
- [7] A. Arcones and F.-K. Thielemann, *Astron. Astrophys. Rev.* **31**, 1 (2023).
- [8] A. E. Lovell, F. M. Nunes, M. Catacora-Rios, and G. B. King, *J. Phys. G: Nucl. Part. Phys.* **48**, 014001 (2021).
- [9] M. Catacora-Rios, G. B. King, A. E. Lovell, and F. M. Nunes, *Phys. Rev. C* **104**, 064611 (2021).
- [10] Z. M. Niu and H. Z. Liang, *Phys. Lett. B* **778**, 48 (2018).
- [11] R. D. Lasserri, D. Regnier, J. P. Ebran, and A. Penon, *Phys. Rev. Lett.* **124**, 162502 (2020).
- [12] M. Raissi, P. Perdikaris, and G. E. Karniadakis, *J. Comput. Phys.* **378**, 686 (2019).
- [13] G. E. Karniadakis, I. G. Kevrekidis, L. Lu, P. Perdikaris, S. Wang, and L. Yang, *Nat. Rev. Phys.* **3**, 422 (2021).
- [14] K. Mills, M. Spanner, and I. Tamblyn, *Phys. Rev. A* **96**, 042113 (2017).
- [15] J. Hermann, Z. Schätzle, and F. Noé, *Nat. Chem.* **12**, 891 (2020).
- [16] R. Hasani, M. Lechner, A. Amini, L. Liebenwein, A. Ray, M. Tschaikowski, G. Teschl, and D. Rus, *Nat. Mach. Intell.* **4**, 992 (2022).
- [17] K. Hornik, M. Stinchcombe, and H. White, *Neural Networks* **2**, 359 (1989).
- [18] S. Hochreiter and J. Schmidhuber, *Neural Comput.* **9**, 1735 (1997).
- [19] M. Lechner, R. Hasani, A. Amini, T. A. Henzinger, D. Rus, and R. Grosu, *Nat. Mach. Intell.* **2**, 642 (2020).
- [20] I. Loshchilov and F. Hutter, arXiv preprint arXiv:1711.05101 (2019).